

Sensitive Valence Structures of $[(\text{pap})_2\text{Ru}(\text{Q})]^n$ ($n = +2, +1, 0, -1, -2$) with Two Different Redox Noninnocent Ligands, $\text{Q} = 3,5\text{-Di-}t\text{-butyl-}$ $N\text{-aryl-}1,2\text{-benzoquinonemonoimine}$ and $\text{pap} = 2\text{-Phenylazopyridine}$ [†]

Dipanwita Das,[‡] Tapan Kumar Mondal,[§] Shaikh M. Mobin,[‡] and Goutam Kumar Lahiri*,[‡]

[‡]Department of Chemistry, Indian Institute of Technology Bombay, Powai, Mumbai-400076, India, and

[§]Department of Chemistry, Jadavpur University, Jadavpur, Kolkata-700032, India

Received July 10, 2009

The complexes $[(\text{pap})_2\text{Ru}(\text{Q})]\text{ClO}_4$, $[\mathbf{1}]\text{ClO}_4^-$ – $[\mathbf{4}]\text{ClO}_4^-$, with two different redox noninnocent ligands, $\text{Q} = 3,5\text{-di-}t\text{-butyl-}$
 $N\text{-aryl-}1,2\text{-benzoquinonemonoimine}$ (-aryl = *m*-(Cl)₂C₆H₃(1^+), C₆H₅(2^+), *m*-(OCH₃)₂C₆H₃(3^+), and *m*-(^tBu)₂C₆H₃(4^+))
and pap = 2-phenylazopyridine, have been synthesized and characterized using various analytical techniques. The single-crystal X-ray structure of the representative $[\mathbf{2}]\text{ClO}_4^- \cdot \text{C}_7\text{H}_8$ exhibits multiple intermolecular C–H · · · O hydrogen bondings and C–H · · · π interactions. The C1–O1 = 1.287(4) (density functional theory, DFT, 1.311) and C6–N1 = 1.320(4) (DFT, 1.353) Å and intraring bond distances associated with the sensitive quinine (Q) moiety along with the azo(pap) bond distances, N3–N4 = 1.278(4) (DFT, 1.297) and N6–N7 = 1.271(4) (DFT, 1.289) Å, in $\mathbf{2}^+$ justify the $[(\text{pap})_2\text{Ru}^{II}(\text{Q}^\bullet^-)]^+$ valence configuration at the native state of $1^+ - 4^+$. Consequently, Mulliken spin densities on Q, pap, and Ru in $\mathbf{2}^+$ are calculated to be 0.8636, 0.1040, and 0.0187, respectively, and $1^+ - 4^+$ exhibit free radical sharp EPR spectra and one weak and broad transition around 1000 nm in CH₃CN due to interligand transition involving a singly occupied molecular orbital (SOMO) of Q^{•-} and the vacant π* orbital of pap. Compounds $1^+ - 4^+$ undergo a quasi-reversible oxidation and three successive reductions. The valence structure of the electron paramagnetic resonance (EPR)-inactive oxidized state in $1^{2+} - 4^{2+}$ has been established as $[(\text{pap})_2\text{Ru}^{II}(\text{Q}^\circ)]^{2+}$ instead of the alternate formalism of antiferromagnetically coupled $[(\text{pap})_2\text{Ru}^{III}(\text{Q}^\bullet^-)]^{2+}$ on the basis of the DFT calculations on the optimized $\mathbf{2}^+$, which predict that the singly occupied molecular orbital is primarily composed of Q with 77% contribution. Accordingly, the optimized structure of $\mathbf{2}^{2+}$ predicts shorter C1–O1 (1.264) and C6–N1 (1.317 Å) distances and longer Ru1–O1 (2.080) and Ru1–N1 (2.088 Å) distances. Compounds $1^{2+} - 4^{2+}$ exhibit the lowest energy transitions around 600 nm, corresponding to Ru(dπ)/Q(π) → pap(π*). The presence of two sets of strongly π-acceptor ligands, pap and Q, in $1^{2+} - 4^{2+}$ stabilizes the Ru(II) state to a large extent such that the further oxidation of {Ru^{II}–Q[°]} → {Ru^{III}–Q[°]} has not been detected within +2.0 V versus a saturated calomel electrode. The EPR-inactive reduced states $1^- - 4^-$ have been formulated as $[(\text{pap})_2\text{Ru}^{II}(\text{Q}^{2-})]$ over the antiferromagnetically coupled alternate configuration, $[(\text{pap})(\text{pap}^\bullet^-)\text{Ru}^{II}(\text{Q}^\bullet^-)]$. The optimized structure of $\mathbf{2}$ predicts sensitive C1–O1 and C6–N1 bond distances of 1.337 and 1.390 Å, respectively, close to the doubly reduced Q²⁻ state, whereas the N=N distances of pap, N3–N4 = 1.299 and N6–N7 = 1.306 Å, remain close to the neutral state. In corroboration with the doubly reduced Q²⁻ state, $1^- - 4^-$ exhibit a moderately strong interligand π(Q²⁻) → π*(pap) transition in the near-IR region near 1300 nm. The subsequent two reductions are naturally centered around the azo functions of the pap ligands.

Introduction

The recognition of sizable mixing of redox-sensitive dπ(Ru) and pπ(quinonoid, Q) frontier orbitals has initiated continuous efforts in establishing the valence state distribution aspects at the metal–quinonoid interface using newer molecular frameworks.^{1–6} Furthermore, the recent reports related to the application potentials of ruthenium–quinonoid derivatives in the water oxidation process⁷ extend additional impetus in dealing with such complexes. It often

introduces a challenging or a rather confusing scenario in determining the precise metal–ligand valence state distributions in accessible redox states.⁸ Moreover, the superposition of resonating states in ruthenium–quinonoid systems may also lead to the yielding of the intermediate description, as stated by Remenyi and Kaupp.⁹ A wide variety of mono-nuclear complexes of the general composition $[(\text{AL}^p)\text{Ru}^q(\text{Q}^m)]^n$ (AL = ancillary ligand; Q = quinonoid framework; *p*, *q*, *m*, and *n* are the respective charges; Scheme 1) have been studied in detail, and substantial variations in the valence distribution profile of such complexes have been reported on the basis of even simple alterations of the electronic nature of either AL or Q,^{1–9} revealing the need for further investiga-

[†]Dedicated to Professor Animesh Chakravorty on the eve of his 75th birthday.

*To whom correspondence should be addressed. E-mail: lahiri@chem.iitb.ac.in.

tions of this delicate valence phenomenon with the newer combinations in $[(AL^P)Ru^Q(Q'')]^{n-}$. Though a large number of mononuclear ruthenium-Q derivatives have been designed along with a wide variety of coligands (Scheme 1) over the past few decades, only one report of a ruthenium-Q ($Q: X=Y=O$, Scheme 1) derivative in combination with $AL = pap$ ($pap = 2\text{-phenylazopyridine}$) is known so far.^{8d} Further, a $\{\text{Ru}-Q\}$ derivative where Q is comprised of

- (1) (a) Poddel'sky, A. I.; Cherkasov, V. K.; Abakumov, G. A. *Coord. Chem. Rev.* **2009**, 253, 291. (b) Zanello, P.; Corsini, M. *Coord. Chem. Rev.* **2006**, 250, 2000. (c) Butin, K. P.; Beloglazkina, E. K.; Zykl, N. V. *Russ. Chem. Rev.* **2005**, 74, 531. (d) Gorelsky, S. I.; Lever, A. B. P.; Ebadi, M. *Coord. Chem. Rev.* **2002**, 230, 97. (e) Pierpont, C. G. *Coord. Chem. Rev.* **2001**, 219–221, 415. (f) Lever, A. B. P.; Gorelsky, S. I. *Coord. Chem. Rev.* **2000**, 208, 153. (g) Gorelsky, S. I.; Dodsworth, E. S.; Lever, A. B. P.; Vlcek, A. A. *Coord. Chem. Rev.* **1998**, 174, 469. (h) Pierpont, C. G.; Lange, C. W. *Prog. Inorg. Chem.* **1994**, 41, 331. (i) Vlcek, A., Jr. *Comments Inorg. Chem.* **1994**, 16, 207. (j) Lever, A. B. P.; Masui, H.; Metcalfe, R. A.; Stukens, D. J.; Dodsworth, E. S.; Auburn, P. R. *Coord. Chem. Rev.* **1993**, 125, 317. (k) Juris, A.; Balzani, V.; Barigelletti, F.; Campagna, S.; Belser, P.; von Zelewsky, A. *Coord. Chem. Rev.* **1988**, 84, 85. (l) Kaim, W. *Coord. Chem. Rev.* **1987**, 76, 187. (m) Girgis, A. Y.; Sohn, Y. S.; Balch, A. L. *Inorg. Chem.* **1975**, 14, 2327.

- (2) (a) Haga, M.; Dodsworth, E. S.; Lever, A. B. P. *Inorg. Chem.* **1986**, 25, 447. (b) Masui, H.; Lever, A. B. P.; Auburn, P. *Inorg. Chem.* **1991**, 30, 2402. (c) Ebadi, M.; Lever, A. B. P. *Inorg. Chem.* **1999**, 38, 467. (d) Lever, A. B. P.; Auburn, P. R.; Dodsworth, E. S.; Haga, M.; Liu, W.; Melnik, M.; Nevin, W. A. *J. Am. Chem. Soc.* **1988**, 110, 8076. (e) Auburn, P. R.; Dodsworth, E. S.; Haga, M.; Liu, W.; Nevin, W. A.; Lever, A. B. P. *Inorg. Chem.* **1991**, 30, 3502. (f) Lever, A. B. P.; Gorelsky, S. L. *Struct. Bonding (Berlin)* **2004**, 107, 77. (g) Masui, H.; Lever, A. B. P.; Dodsworth, E. S. *Inorg. Chem.* **1993**, 32, 258. (h) Metcalfe, R. A.; Lever, A. B. P. *Inorg. Chem.* **1997**, 36, 4762. (i) Rusanova, J.; Rusanov, E.; Gorelsky, S. I.; Christendat, D.; Popescu, R.; Farah, A. A.; Beaulac, R.; Reber, C.; Lever, A. B. P. *Inorg. Chem.* **2006**, 45, 6246. (j) DelMedico, A.; Dodsworth, E. S.; Lever, A. B. P.; Pietro, W. J. *Inorg. Chem.* **2004**, 43, 2654. (k) da Cunha, C. J.; Dodsworth, E. S.; Monteiro, M. A.; Lever, A. B. P. *Inorg. Chem.* **1999**, 38, 5399.

- (3) (a) Bhattacharya, S.; Boone, S. R.; Fox, G. A.; Pierpont, C. G. *J. Am. Chem. Soc.* **1990**, 112, 1088. (b) Bhattacharya, S.; Pierpont, C. G. *Inorg. Chem.* **1991**, 30, 1511. (c) Haga, M.; Dodsworth, E. S.; Lever, A. B. P.; Boone, S. R.; Pierpont, C. G. *J. Am. Chem. Soc.* **1986**, 108, 7413. (d) Boone, S. R.; Pierpont, C. G. *Inorg. Chem.* **1987**, 26, 1769. (e) Bhattacharya, S.; Pierpont, C. G. *Inorg. Chem.* **1994**, 33, 6038. (f) Haga, M.; Isobe, K.; Boone, S. R.; Pierpont, C. G. *Inorg. Chem.* **1990**, 29, 3795.

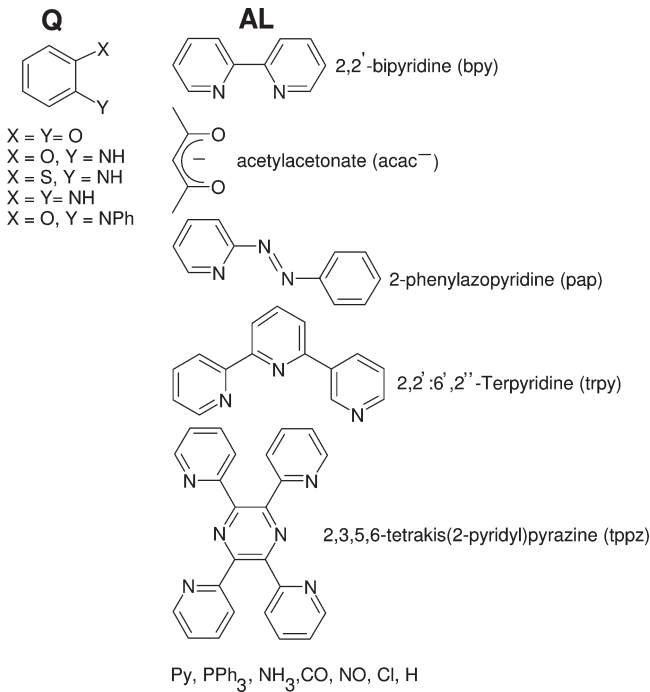
- (4) (a) Mitra, K. N.; Majumdar, P.; Peng, S. M.; Castineiras, A.; Goswami, S. *Chem. Commun.* **1997**, 1267. (b) Mitra, K. N.; Choudhury, S.; Castineiras, A.; Goswami, S. *J. Chem. Soc., Dalton Trans.* **1998**, 2901. (c) Das, C.; Kumar, K. K.; Ghosh, A. K.; Majumdar, P.; Hung, C.-H.; Goswami, S. *New J. Chem.* **2002**, 26, 1409.

- (5) (a) Waldhör, E.; Schwederski, B.; Kaim, W. *J. Chem. Soc., Perkin Trans. 2* **1993**, 2109. (b) Ernst, S.; Hänel, P.; Jordanov, J.; Kaim, W.; Kasack, V.; Roth, E. *J. Am. Chem. Soc.* **1989**, 111, 1733. (c) Ernst, S.; Kasack, V.; Bessenbacher, C.; Kaim, W. Z. *Naturforsch.* **1987**, 42b, 425. (d) Kasack, V.; Kaim, W.; Binder, H.; Jordanov, J.; Roth, E. *Inorg. Chem.* **1995**, 34, 1924. (e) Knödler, A.; Fiedler, J.; Kaim, W. *Polyhedron* **2004**, 23, 701.

- (6) (a) Okamura, R.; Wada, T.; Aikawa, K.; Nagata, T.; Tanaka, K. *Inorg. Chem.* **2004**, 43, 7210. (b) Kurihara, M.; Daniele, S.; Tsuge, K.; Sugimoto, H.; Tanaka, K. *Bull. Chem. Soc. Jpn.* **1998**, 71, 867. (c) Ward, M. D.; McCleverty, J. A. *J. Chem. Soc., Dalton Trans.* **2002**, 275. (d) Dei, A.; Gatteschi, D.; Pardi, L. *Inorg. Chem.* **1990**, 29, 1442. (e) Hino, T.; Wada, T.; Fujihara, T.; Tanaka, K. *Chem. Lett.* **2004**, 33, 1596. (f) Miyazato, Y.; Wada, T.; Muckerman, J. T.; Fujita, E.; Tanaka, K. *Angew. Chem., Int. Ed.* **2007**, 46, 5728. (g) Miyazato, Y.; Wada, T.; Tanaka, K. *Bull. Chem. Soc. Jpn.* **2006**, 79, 745. (h) Tsuge, K.; Kurihara, M.; Tanaka, K. *Bull. Chem. Soc. Jpn.* **2000**, 73, 607. (i) Kobayashi, K.; Ohtsu, H.; Wada, T.; Kato, T.; Tanaka, K. *J. Am. Chem. Soc.* **2003**, 125, 6729. (j) Tsuge, K.; Tanaka, K. *Chem. Lett.* **1998**, 1069. (k) Ward, M. D. *Inorg. Chem.* **1996**, 35, 1712. (l) Meacham, A. P.; Druce, K. L.; Bell, Z. R.; Ward, M. D.; Keister, J. B.; Lever, A. B. P. *Inorg. Chem.* **2003**, 42, 7887. (m) Barthram, A. M.; Cleary, R. L.; Kowallick, R.; Ward, M. D. *Chem. Commun.* **1998**, 2695. (n) Joss, S.; Reust, H.; Ludi, A. *J. Am. Chem. Soc.* **1981**, 103, 981. (o) Keyes, T. E.; Forster, R. J.; Jayaweera, P. M.; Coates, C. G.; McGarvey, J. J.; Vos, J. G. *Inorg. Chem.* **1998**, 37, 5925. (p) Bhattacharya, S. *Polyhedron* **1994**, 13, 451.

- (7) (a) Muckerman, J. T.; Polynsky, D. E.; Wada, T.; Tanaka, K.; Fujita, E. *Inorg. Chem.* **2008**, 47, 1787. (b) Wada, T.; Tsuge, K.; Tanaka, K. *Inorg. Chem.* **2001**, 40, 329. (c) Wada, T.; Tsuge, K.; Tanaka, K. *Angew. Chem., Int. Ed.* **2000**, 39, 1479. (d) Tsai, M. K.; Rochford, J.; Polynsky, D. E.; Wada, T.; Tanaka, K.; Fujita, E.; Muckerman, T. J. *Inorg. Chem.* **2009**, 48, 4372.

Scheme 1



X = O and Y = NPh (Scheme 1) has been limited to only a few studies along with AL = bpy (2,2'-bipyridine),¹⁰ terpy (2,2':6'2''-terpyridine),¹¹ and tppz (2,3,5,6 tetrakis(2-pyridyl)-pyrazine),¹² though many articles have appeared in recent years with the other transition elements.^{1a,13} Considering the sensitive roles of the electronic nature of both AL and Q on the valence configuration of {AL-Ru-Q}, the present study is directed toward the hitherto unexplored combina-

- (8) (a) Patra, S.; Sarkar, B.; Mobin, S. M.; Kaim, W.; Lahiri, G. K. *Inorg. Chem.* **2003**, 42, 6469. (b) Maji, S.; Patra, S.; Chakraborty, S.; Janardanan, D.; Mobin, S. M.; Sunoj, R. B.; Lahiri, G. K. *Eur. J. Inorg. Chem.* **2007**, 314. (c) Ghumaan, S.; Sarkar, B.; Maji, S.; Puranik, V. G.; Fiedler, J.; Urbanos, F. A.; Jimenez-Aparicio, R.; Kaim, W.; Lahiri, G. K. *Chem.—Eur. J.* **2008**, 14, 10816. (d) Bag, N.; Pramanik, A.; Lahiri, G. K.; Chakravorty, A. *Inorg. Chem.* **1992**, 31, 40. (e) Bag, N.; Lahiri, G. K.; Basu, P.; Chakravorty, A. *J. Chem. Soc., Dalton Trans.* **1992**, 113. (f) Patra, S.; Sarkar, B.; Ghumaan, S.; Fiedler, J.; Zalis, S.; Kaim, W.; Lahiri, G. K. *J. Chem. Soc., Dalton Trans.* **2004**, 750. (g) Maji, S.; Sarkar, B.; Mobin, S. M.; Fiedler, J.; Urbanos, F. A.; Jimenez-Aparicio, R.; Kaim, W.; Lahiri, G. K. *Inorg. Chem.* **2008**, 47, 5204. (h) Kumbhakar, D.; Sarkar, B.; Maji, S.; Mobin, S. M.; Fiedler, J.; Urbanos, F. A.; Jimenez-Aparicio, R.; Kaim, W.; Lahiri, G. K. *J. Am. Chem. Soc.* **2008**, 130, 17575. (i) Chakraborty, S.; Laye, R. H.; Paul, R. L.; Gonnade, R. G.; Puranik, V. G.; Ward, M. D.; Lahiri, G. K. *J. Chem. Soc., Dalton Trans.* **2002**, 1172.

- (9) Remenyi, C.; Kaupp, M. *J. Am. Chem. Soc.* **2005**, 127, 11399.

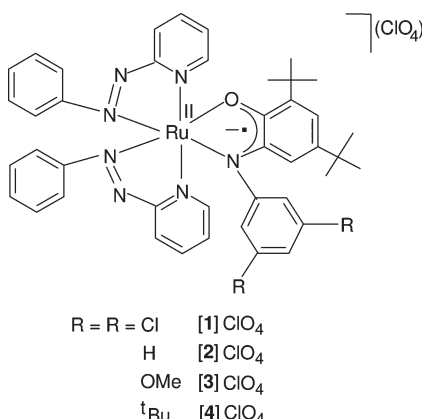
- (10) Ye, S.; Sarkar, B.; Duboc, C.; Fiedler, J.; Kaim, W. *Inorg. Chem.* **2005**, 44, 2843.

- (11) Das, A. K.; Sarkar, B.; Duboc, C.; Strobel, S.; Fiedler, J.; Zalis, S.; Lahiri, G. K.; Kaim, W. *Angew. Chem., Int. Ed.* **2009**, 48, 4242.

- (12) Das, A. K.; Sarkar, B.; Fiedler, J.; Zalis, S.; Hartenbach, I.; Strobel, S.; Lahiri, G. K.; Kaim, W. *J. Am. Chem. Soc.* **2009**, 131, 8895.

- (13) (a) Herebian, D.; Bothe, E.; Bill, E.; Weyhermüller, T.; Wieghardt, K. *J. Am. Chem. Soc.* **2001**, 123, 10012. (b) Chaudhuri, P.; Verani, C. N.; Bill, E.; Bothe, E.; Weyhermüller, T.; Wieghardt, K. *J. Am. Chem. Soc.* **2001**, 123, 2213. (c) Chun, H.; Bill, E.; Bothe, E.; Weyhermüller, T.; Wieghardt, K. *Inorg. Chem.* **2002**, 41, 5091. (d) Ray, K.; Petrenko, T.; Wieghardt, K.; Neese, F. *Dalton Trans.* **2007**, 1552. (e) Chlopek, K.; Bothe, E.; Neese, F.; Weyhermüller, T.; Wieghardt, K. *Inorg. Chem.* **2006**, 45, 6298. (f) Chun, H.; Verani, C. N.; Chaudhuri, P.; Bothe, E.; Bill, E.; Weyhermüller, T.; Wieghardt, K. *Inorg. Chem.* **2001**, 40, 4157. (g) Verani, C. N.; Gallert, S.; Bill, E.; Weyhermüller, T.; Wieghardt, K.; Chaudhuri, P. *Chem. Commun.* **1999**, 1747. (h) Mukherjee, S.; Weyhermüller, T.; Bill, E.; Wieghardt, K.; Chaudhuri, P. *Inorg. Chem.* **2005**, 44, 7099. (i) Chaudhuri, P.; Wagner, R.; Pieper, U.; Biswas, B.; Weyhermüller, T. *Dalton Trans.* **2008**, 1286.

Scheme 2



tion of $[(\text{pap})_2\text{Ru}(\text{Q})]^n$ encompassing two different redox noninnocent ligand centers, Q with $\text{X} = \text{O}$ and $\text{Y} = \text{NPh}$ and $\text{pap} = 2\text{-phenylazopyridine}$, as shown in Scheme 1. The selective induction of “pap” as the AL with the $\{\text{Ru}=\text{Q}\}$ in $[(\text{pap})_2\text{Ru}(\text{Q})]^n$ introduces an additional competitive scenario, as the low-lying $\pi^*(\text{N}=\text{N})$ orbitals of pap are known to undergo facile electron uptake processes at relatively low potentials comparable to that of Q .^{8d,14}

The present article therefore describes the synthesis and characterization of a group of four complexes $[(\text{pap})_2\text{Ru}^{\text{II}}(\text{Q})]^n$ (**1**ⁿ–**4**ⁿ; Q = substituted 3,5-di-*tert*-butyl-*N*-aryl-*o*-iminobenzonitrile; Scheme 2) including the crystal structure of the representative **[2]ClO₄**. The sensitive valence structures of **1**ⁿ–**4**ⁿ ($n = +2, +1, 0, -1, -2$) have been examined via experimental and theoretical investigations.

Results and Discussion

The complexes $[(\text{pap})_2\text{Ru}(\text{Q})]^+ (\mathbf{1}^+-\mathbf{4}^+)$; $\text{pap} = 2\text{-phenylazopyridine}$, $\text{Q} = 3,5\text{-di-}tert\text{-butyl-}N\text{-aryl-}1,2\text{-benzoquinonemonoimine}$ have been synthesized from the precursor complex $ctc\text{-}[\text{Ru}^{\text{II}}(\text{pap})_2(\text{EtOH})_2]^{2+}$ (*ctc* = cis-trans-cis with respect to EtOH and pyridine and azo nitrogens of pap, respectively) and substituted 2-anilino-4,6-di-*tert*-butylphenol(H_2Q) (Scheme 2) in the presence of NEt_3 as a base in refluxing EtOH under a dinitrogen atmosphere. The isolated perchlorate salts, **[1]ClO₄**–**[4]ClO₄**, have been purified using a silica gel column with a $\text{CH}_2\text{Cl}_2\text{-CH}_3\text{CN}$ mixture in a 5:1 ratio as the eluent (see the Experimental Section). The crystal structure of the representative **[2]ClO₄** establishes that the *tc*-configuration of the starting $\{\text{Ru}(\text{pap})_2\}$ moiety¹⁵ has been retained.

The 1:1 conducting complexes give satisfactory microanalytical data. The $\nu(\text{ClO}_4)$ vibrations of **[1]ClO₄**–**[4]ClO₄** expectedly appear near 1100/625 cm^{-1} . The electrospray mass spectra of **[1]ClO₄**–**[4]ClO₄** in CH_3CN show molecular ion peaks (m/z) corresponding to **1**⁺–**4**⁺ (see the Experimental Section). In the solid state, **[1]ClO₄**–**[4]ClO₄** exhibit a magnetic moment μ_{eff} of 1.8–1.9 μ_{B} corresponding to one unpaired electron ($S = 1/2$ ground state). Consequently, the complexes show sharp free-radical electron paramagnetic resonance (EPR) spectra at $g \sim 1.99$ (line width, ~ 9 G) without any detectable hyperfine splitting both in the solid

(14) (a) Maji, S.; Sarkar, B.; Mobin, S. M.; Fiedler, J.; Kaim, W.; Lahiri, G. K. *Dalton Trans.* **2007**, 2411. (b) Patra, S.; Sarkar, B.; Maji, S.; Fiedler, J.; Urbanos, F. A.; Jimenez-Aparicio, R.; Kaim, W.; Lahiri, G. K. *Chem.—Eur. J.* **2006**, 12, 489.

(15) Seal, A.; Ray, S. *Acta Crystallogr., Sect. C* **1984**, 49, 929.

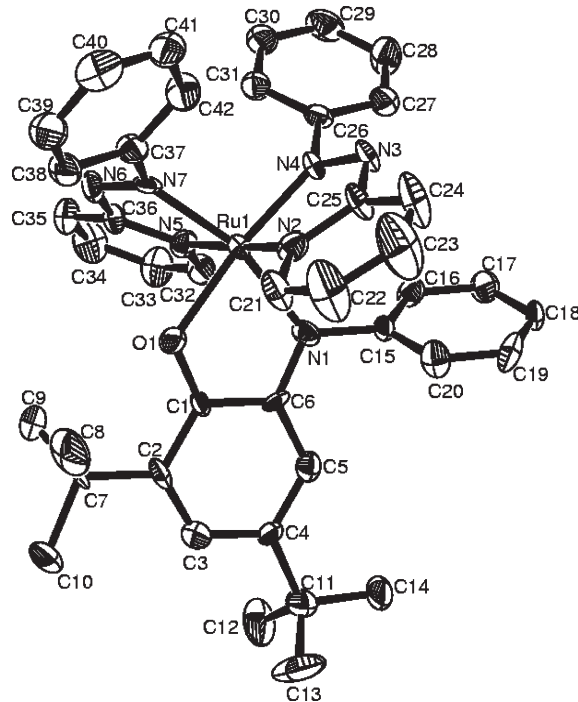


Figure 1. ORTEP plot of the cation of **[2]ClO₄·C₇H₈**. Ellipsoids are drawn with 50% probability.

and solution (CH_3CN) states at 298 K as well as at 77 K (liquid nitrogen; Figure S1, Supporting Information).

The redox-sensitive features of all the three entities, $\text{Ru}(\text{Ru}^{\text{II}}, \text{Ru}^{\text{III}}, \text{Ru}^{\text{IV}})$,¹⁶ pap [$(\text{N}=\text{N})^\circ, (\text{N}-\text{N})^{\bullet-}, (\text{N}-\text{N})^{2-}$],¹⁷ and $\text{Q}(\text{Q}^\circ, \text{Q}^{\bullet-}, \text{Q}^{2-})$ ¹¹ in $[(\text{pap})_2\text{Ru}(\text{Q})]^+ (\mathbf{1}^+-\mathbf{4}^+)$ bring the possibility of multiple reasonable valence structure alternatives in the native state itself. However, the sharp EPR spectra of isolated **1**⁺–**4**⁺ without any nitrogen (I of $^{14}\text{N} = 1$) hyperfine splitting¹⁸ or $\text{Ru}(\text{III})$ ($S = 1/2$) anisotropic contribution¹⁹ (Figure S1, Supporting Information) imply that the native state exists primarily in the $\{(\text{pap})_2\text{Ru}^{\text{II}}-(\text{Q}^{\bullet-})\}$ configuration with the unpaired spin on the redox-sensitive semiquinone ($\text{Q}^{\bullet-}$) moiety.

The native state formulation of $\{(\text{pap})_2\text{Ru}^{\text{II}}(\text{Q}^{\bullet-})\}$ in the solid states of **[1]ClO₄**–**[4]ClO₄**) has been authenticated by the single-crystal X-ray structure of the representative **[2]ClO₄** (Figure 1, Tables 1 and 2). The sensitive bond distances associated with the Q in **[2]ClO₄**, $\text{C}1-\text{O}1 = 1.287(4)$ and $\text{C}6-\text{N}1 = 1.320(4)$, and intraradical bond distances,

(16) (a) Kar, S.; Sarkar, B.; Ghumaan, S.; Roy, D.; Urbanos, F. A.; Fiedler, J.; Sunoj, R. B.; Jimenez-Aparicio, R.; Kaim, W.; Lahiri, G. K. *Inorg. Chem.* **2005**, 44, 8715. (b) Bhattacharya, S.; Chakravorty, A.; Cotton, F. A.; Mukherjee, R.; Schwotzer, W. *Inorg. Chem.* **1984**, 23, 1709.

(17) (a) Shivakumar, M.; Pramanik, K.; Ghosh, P.; Chakravorty, A. *Inorg. Chem.* **1998**, 37, 5968. (b) Sarkar, B.; Patra, S.; Fiedler, J.; Sunoj, R. B.; Janardanan, D.; Mobin, S. M.; Niemeyer, M.; Lahiri, G. K.; Kaim, W. *Angew. Chem., Int. Ed.* **2005**, 44, 5655. (c) Ghumaan, S.; Mukherjee, S.; Kar, S.; Roy, D.; Mobin, S. M.; Sunoj, R. B.; Lahiri, G. K. *Eur. J. Inorg. Chem.* **2006**, 4426. (d) Sarkar, B.; Patra, S.; Fiedler, J.; Sunoj, R. B.; Janardanan, D.; Lahiri, G. K.; Kaim, W. *J. Am. Chem. Soc.* **2008**, 130, 3532.

(18) Kar, S.; Sarkar, B.; Ghumaan, S.; Janardanan, D.; van Slageren, J.; Fiedler, J.; Puranik, V. G.; Sunoj, R. B.; Kaim, W.; Lahiri, G. K. *Chem.—Eur. J.* **2005**, 11, 4901.

(19) (a) Ghumaan, S.; Kar, S.; Mobin, S. M.; Harish, B.; Puranik, V. G.; Lahiri, G. K. *Inorg. Chem.* **2006**, 45, 2413. (b) Kar, S.; Chanda, N.; Mobin, S. M.; Urbanos, F. A.; Niemeyer, M.; Puranik, V. G.; Jimenez-Aparicio, R.; Lahiri, G. K. *Inorg. Chem.* **2005**, 44, 1571. (c) Kar, S.; Chanda, N.; Mobin, S. M.; Datta, A.; Urbanos, F. A.; Puranik, V. G.; Jimenez-Aparicio, R.; Lahiri, G. K. *Inorg. Chem.* **2004**, 43, 4911.

Table 1. Selected Crystallographic Data for $[2]\text{ClO}_4\cdot\text{C}_7\text{H}_8$

	$[2]\text{ClO}_4\cdot\text{C}_7\text{H}_8$
mol formula	$\text{C}_{49}\text{H}_{51}\text{ClN}_7\text{O}_5\text{Ru}$
fw	954.49
cryst sym	monoclinic
space group	$P\bar{2}1/n$
<i>a</i> (Å)	11.744(8)
<i>b</i> (Å)	19.608(10)
<i>c</i> (Å)	19.557(9)
β (deg)	102.47(5)
<i>V</i> (Å ³)	4397(4)
<i>Z</i>	4
μ (mm ⁻¹)	0.474
<i>T</i> (K)	120(2)
<i>D</i> _{calcd} (g cm ⁻³)	1.442
F (000)	1980
2θ range (deg)	2.98 to 25.00
data/restraints/params	7727/0/575
R1, wR2 [<i>I</i> > 2σ(<i>I</i>)]	0.0409, 0.0836
R1, wR2 (all data)	0.0771, 0.0906
GOF	0.825
largest diff. peak/hole (e Å ⁻³)	0.716 and -0.569

$\text{C}_1-\text{C}_2 = 1.392(5)$, $\text{C}_2-\text{C}_3 = 1.355(5)$, $\text{C}_3-\text{C}_4 = 1.405(5)$, $\text{C}_4-\text{C}_5 = 1.331(5)$, $\text{C}_5-\text{C}_6 = 1.392(5)$ and $\text{C}_6-\text{C}_1 = 1.395(5)$ Å, are in favor of the intermediate radical semiquinonoid (Sq) state, $\text{Q}^{\bullet-}$.²⁰ The N–N bond distances in $[2]\text{ClO}_4$, $\text{N}_3-\text{N}_4 = 1.278(4)$ and $\text{N}_6-\text{N}_7 = 1.271(4)$ Å, match perfectly well with the unreduced ($\text{N}=\text{N}^\circ$) state of pap reported earlier in structurally characterized ruthenium complexes.²¹ However, a $\text{N}=\text{N}$ distance of approximately 1.27 Å in $[2]\text{ClO}_4$ is slightly longer than that reported in the free state of pap, 1.258(5) Å,²² due to a partial shift of charge from the filled $d\pi(\text{Ru}^{II})$ to the low-lying $\pi^*(\text{N}=\text{N})$ in the form of back bonding.²¹ The immediate consequence of $d\pi(\text{Ru}^{II}) \rightarrow \pi^*(\text{N}=\text{N})$ back bonding has been reflected in the shortened $\text{Ru}-\text{N}(\text{azo})$ distances, $\text{Ru}_1-\text{N}_4 = 1.937(3)$ and $\text{Ru}_1-\text{N}_7 = 1.944(3)$ Å, relative to the corresponding $\text{Ru}-\text{N}(\text{pyridine})$ distances, $\text{Ru}_1-\text{N}_2 = 1.982(3)$ and $\text{Ru}_1-\text{N}_5 = 2.000(3)$ Å, of pap ligands. The DFT calculations on the representative $\mathbf{2}^+$ (α spin) predict 13% and 21% Ru contributions in the close-by lowest unoccupied molecular orbital (LUMO) and LUMO+1 along with 81% and 74% pap contributions, respectively (Table 3), also implying the partial mixing of frontier orbitals of the filled $d\pi(\text{Ru})$ with the azo-based vacant π^* orbitals of pap.^{17c,23}

The DFT-optimized structure of $\mathbf{2}^+$ is shown in Figure 2. The calculated bond parameters agree reasonably well with the experimental data, Table 2, revealing the reliability of the optimization process. The calculated relevant bond distances of coordinated Q, $\text{C}_1-\text{O}_1 = 1.311$, $\text{C}_6-\text{N}_1 = 1.353$, $\text{C}_1-\text{C}_2 = 1.418$, $\text{C}_2-\text{C}_3 = 1.384$, $\text{C}_3-\text{C}_4 = 1.425$, $\text{C}_4-\text{C}_5 = 1.351$, $\text{C}_5-\text{C}_6 = 1.418$, and $\text{C}_1-\text{C}_6 = 1.419$ Å, and N–N distances of coordinated pap, $\text{N}_3-\text{N}_4 = 1.297$ and $\text{N}_6-\text{N}_7 = 1.289$ Å, are also in agreement with the $\{(\text{pap})_2\text{Ru}^{II}(\text{Q}^{\bullet-})\}$ configuration for $\mathbf{2}^+$. Consequently, the spin density plot of

(20) Bhattacharya, S.; Gupta, P.; Basuli, F.; Pierpont, C. G. *Inorg. Chem.* **2002**, *41*, 5810.

(21) (a) Santra, B. K.; Thakur, G. A.; Ghosh, P.; Pramanik, A.; Lahiri, G. K. *Inorg. Chem.* **1996**, *35*, 3050. (b) Kar, S.; Pradhan, B.; Sinha, R. K.; Kundu, T.; Kodigure, P.; Rao, K. K.; Puranik, V. G.; Lahiri, G. K. *Dalton Trans.* **2004**, 1752.

(22) Majumdar, P.; Peng, S. M.; Goswami, S. J. *Chem. Soc., Dalton Trans.* **1998**, 1569.

(23) (a) Patra, S.; Sarkar, B.; Ghumaan, S.; Patil, M. P.; Mobin, S. M.; Sunoj, R. B.; Kaim, W.; Lahiri, G. K. *Dalton Trans.* **2005**, 1188. (b) Kalinin, D.; Dares, C.; Kaluarachchi, H.; Potvin, P. G.; Lever, A. B. P. *Inorg. Chem.* **2008**, *47*, 10110.

$\mathbf{2}^+$ (Figure 3) shows that Q is the primary spin-bearing center with Mulliken spin densities of 0.8636, 0.1040, and 0.0187 on Q, pap, and Ru, respectively.²⁴

It should be noted that, in the earlier reported analogous system $[(\text{tap})_2\text{Ru}(\text{Q})]$ ($\text{tap} = 2\text{-tolylazopyridine}$) with Q corresponding to X=Y=O (Scheme 1), the quinonoid moiety gets stabilized preferentially in the dianionic catecholate form in the isolated native state.^{8d} Therefore, slight tuning of the quinonoid framework from Q, X=Y=O to X=O and Y=NAr, as in the present case, introduces a precise difference toward the stability of the redox state of the coordinated Q.

The packing diagram of $[2](\text{ClO}_4)\cdot\text{C}_7\text{H}_8$ along the *a* axis is shown in Figure 4. It exhibits multiple intermolecular C–H···O hydrogen bondings involving (i) pyridine hydrogens of the coordinated pap ligand and oxygen atoms of the perchlorate anion, $\text{C}(32)-\text{H}(32)\cdots\text{O}(222)/\text{C}(33)-\text{H}(33)\cdots\text{O}(444)$, and (ii) oxygen atoms of the perchlorate anion and hydrogen atoms of the methyl group of toluene as well as the pendant N-phenyl ring of Q, $\text{C}(77)-\text{H}(77)\cdots\text{O}(111)/\text{C}(16)-\text{H}(16)\cdots\text{O}(222)$. Furthermore, it shows C–H···π interactions between the remaining two hydrogen atoms of the methyl group of toluene and the pyridine ring of one of the pap ligands as well as with the benzene ring of Q (Figure 4, Table 4).

In CH_3CN , $\mathbf{1}^+-\mathbf{4}^+$ exhibit one moderately intense transition near 660 nm and two close-by partially overlapping bands between 570 and 530 nm along with multiple intense transitions in the UV region. In addition, one broad band at the much lower energy part near 1000 nm has been systematically resolved for all of the complexes. The position and intensity of the bands vary slightly depending on the electronic nature of the substituents, R in the pendant phenyl ring of Q (Figure 5, Table 5). The low-energy broad transition around 1000 nm is considered to be the interligand transition from the singly occupied state of $\text{Q}^{\bullet-}$ to the low-lying vacant π^* orbital of pap, as the singly occupied molecular orbital (SOMO) and LUMO/LUMO+1 (α spin) are primarily composed of Q (77%) and pap (81)/(74)% respectively (Table 3). The time-dependent density functional theory (TDDFT) calculations on the optimized structure of the representative $\mathbf{2}^+$ also predict the low-energy transition, λ/nm ($\epsilon/\text{M}^{-1}\text{cm}^{-1}$), at 998.4 (2676) corresponding to $\text{SOMO}(\alpha) \rightarrow \text{LUMO}+1(\alpha)$ and $\text{Q}(\pi) \rightarrow \text{pap}(\pi^*)$, which matches fairly well with the experimental band at 1003 (1290) (Tables 3, 5, and 6, Figures 5 and 6). In addition, TDDFT calculations predict one more low-energy transition at 1328.8 (2921) due to the $\text{SOMO}(\alpha) \rightarrow \text{LUMO}(\alpha)$ and $\text{Q}(\pi) \rightarrow \text{pap}(\pi^*)$ transition; however, this has not been resolved in the spectrum of $\mathbf{2}^+$ (Tables 5 and 6 and Figure 5). The π-acceptor character of pap results in a decrease in energy of LUMOs (LUMO and LUMO+1), or in other words, the energy difference between the SOMO and LUMO decreases drastically, which in turn facilitates the $\text{Q}(\pi) \rightarrow \text{pap}(\pi^*)$ interligand transition occurring at the isolated lower-energy region near 1000 nm. In the analogous $[\text{Ru}^{II}(\text{bpy})_2\text{Q}^{\bullet-}]^+$ derivative (bpy = 2,2'-bipyridine, Q: X = O, Y = NPh, Scheme 1), the mentioned interligand transition is reported to appear at a much higher energy of 687 nm,¹⁰ primarily due to the weaker π-acceptor character of bpy with respect to pap.²⁵ The visible energy transitions are interpreted

(24) Milsmann, C.; Patra, G. K.; Bill, E.; Weyhermüller, T.; George, S. D.; Wieghardt, K. *Inorg. Chem.* **2009**, *48*, 7430.

(25) Mondal, B.; Paul, H.; Puranik, V. G.; Lahiri, G. K. *J. Chem. Soc., Dalton Trans.* **2001**, 481.

Table 2. Selected Experimental Bond Distances (\AA) and Angles (deg) for [2]ClO₄ and Calculated Bond Parameters for $\mathbf{2}^+$, $\mathbf{2}^{2+}$, and $\mathbf{2}$

bond distances	exptl (X-ray)	calcd (DFT)		
		$\mathbf{2}^+$	$\mathbf{2}^{2+}$	$\mathbf{2}$
Ru(1)–O(1)	1.996(3)	2.036	2.080	2.023
Ru(1)–N(1)	2.002(3)	2.036	2.088	2.050
Ru(1)–N(2)	1.982(3)	2.024	2.069	2.012
Ru(1)–N(4)	1.937(3)	1.977	2.058	2.017
Ru(1)–N(5)	2.000(3)	2.031	2.076	2.039
Ru(1)–N(7)	1.944(3)	1.976	2.069	2.018
C(1)–O(1)	1.287(4)	1.311	1.264	1.337
C(6)–N(1)	1.320(4)	1.353	1.317	1.390
N(3)–N(4)	1.278(4)	1.297	1.274	1.299
N(6)–N(7)	1.271(4)	1.289	1.269	1.306
C(1)–C(2)	1.392(5)	1.418	1.427	1.407
C(2)–C(3)	1.355(5)	1.384	1.363	1.394
C(3)–C(4)	1.405(5)	1.425	1.443	1.408
C(4)–C(5)	1.331(5)	1.351	1.358	1.393
C(5)–C(6)	1.392(5)	1.418	1.440	1.415
C(6)–C(1)	1.395(5)	1.419	1.460	1.432
C(15)–N(1)	1.410(4)	1.433	1.420	1.416

bond angles	exptl	calcd		
		$\mathbf{2}^+$	$\mathbf{2}^{2+}$	$\mathbf{2}$
O(1)–Ru(1)–N(7)	85.33(11)	85.23	87.85	83.14
O(1)–Ru(1)–N(4)	171.65(11)	171.7	170.8	169.4
O(1)–Ru(1)–N(5)	83.17(12)	83.19	83.93	84.13
O(1)–Ru(1)–N(1)	78.57(11)	78.47	76.75	79.52
O(1)–Ru(1)–N(2)	96.42(12)	96.19	95.89	93.72
N(2)–Ru(1)–N(7)	100.25(12)	100.0	100.1	100.6
N(2)–Ru(1)–N(4)	76.51(13)	76.79	75.96	76.06
N(2)–Ru(1)–N(5)	176.84(12)	176.88	175.9	176.5
N(2)–Ru(1)–N(1)	87.38(12)	87.65	87.00	89.46
N(1)–Ru(1)–N(5)	95.59(12)	95.21	96.92	92.82
N(1)–Ru(1)–N(4)	96.48(12)	96.65	98.31	97.23
N(1)–Ru(1)–N(7)	162.89(12)	162.6	163.6	161.1
N(4)–Ru(1)–N(5)	104.14(13)	104.0	104.5	106.2
N(7)–Ru(1)–N(5)	76.60(12)	76.85	75.75	76.45
N(7)–Ru(1)–N(4)	100.17(12)	100.2	97.67	100.7

in terms of TDDFT calculations, which predict three moderately intense transitions, λ/nm ($\epsilon/\text{M}^{-1} \text{ cm}^{-1}$), at 652.5(1003), 549.3(8718), and 541.0(8986) [experimental: 665(6820), 565(11100), and 528(11100)] corresponding to HOMO–1(α) \rightarrow LUMO(α)/LUMO+1(α), Ru(d π)/Q(π) \rightarrow pap(π^*)/HOMO–2(α) \rightarrow LUMO(α), Ru(d π)/pap(π) \rightarrow pap(π^*); HOMO–2(β)/HOMO–3(β) \rightarrow LUMO(β)/LUMO+1(β), Ru(d π) \rightarrow pap(π^*)/HOMO–1(β) \rightarrow LUMO(β), Ru(d π)/pap(π) \rightarrow pap(π^*); and HOMO–2(β) \rightarrow LUMO(β)/LUMO+2(β), Ru(d π) \rightarrow pap(π^*), respectively (Table 6, Figure 6). The presence of three close-by pap-dominated LUMOs in the β spin (LUMO, LUMO+1, and LUMO+2; Table 3) facilitates the appearance of two partially overlapping metal-to-ligand charge-transfer bands near 550 nm. The HOMOs are also in mixed metal–ligand composite states (Table 3), as conceivable in the complexes, $\mathbf{1}^+-\mathbf{4}^+$, with two sets of non-innocent ligands, Q and pap.

The complexes $\mathbf{1}^+-\mathbf{4}^+$ exhibit four-step, one-electron each, quasi-reversible redox processes in the potential range of ± 2.0 V versus saturated calomel electrode (SCE; Figure 7, Table 7). The potentials of one oxidative (I) and three successive reductive couples (II–IV) vary reasonably depending on the electron-withdrawing or electron-donating properties of R present in the framework of Q, and it follows the order of $\mathbf{4}^+ < \mathbf{3}^+ < \mathbf{2}^+ < \mathbf{1}^+$ systematically for all of the couples, I–IV (Table 7). The separation in potential between the successive couples results in moderately high

comproportionation constant (K_c , $RT \ln K_c = nF(\Delta E)^{26}$) values in the range of 10^8 to 10^{11} , implying appreciable stability of the intermediate redox states on the cyclic voltammetric time scale. The coulometrically generated one-electron oxidized, green, $\mathbf{1}^{2+}-\mathbf{4}^{2+}$ as well as one-electron reduced, pink, $\mathbf{1}-\mathbf{4}$ are quite stable at 298 K and can be reversibly reduced and reoxidized, respectively, to the parent $\mathbf{1}^+-\mathbf{4}^+$. However, coulometrically generated second ($\mathbf{1}^--\mathbf{4}^-$) and third ($\mathbf{1}^{2-}-\mathbf{4}^{2-}$) reduced states are found to be unstable at 298 K, though the corresponding couples, III and IV (Figure 7), exhibit reversibility on the cyclic voltammetric time scale. The analogous bpy complex exhibits two oxidation and one reduction couple, $E^\circ_{298}, \text{V}(\text{CH}_2\text{Cl}_2/0.1 \text{ M Bu}_4\text{NPF}_6)$, at 1.22/–0.42 and –1.29, respectively, versus $\text{Fe}(\text{C}_5\text{H}_5)_2^{+/0}$ (1.67/0.03 and –0.84 versus SCE).¹⁰ Therefore, an appreciable positive shift of the first oxidation and reduction couples (Table 7) takes place on switching from the bpy coligand to the stronger π -accepting pap ligand in the corresponding unsubstituted $\mathbf{2}^+$. As a consequence to this significant difference in π -accepting strength between pap and bpy, the expected second oxidation process does not appear in $\mathbf{2}^+$ (estimated potential, > 2.0 V versus SCE with respect to the bpy analogue) within the potential limit of +2.0 V in CH₃CN versus SCE; however, two additional reductions, couples III and IV, appear within –2.0 V (Table 7, Figure 7).

Table 3. Selected Molecular Orbitals Along with their Energies and Compositions for $[2]^+$

MO	energy, eV	composition		
		Ru	Pap	Q
α spin				
LUMO+5	-2.66	08	87	05
LUMO+4	-2.72	14	49	37
LUMO+3	-3.66	04	95	01
LUMO+2	-3.74	03	97	0
LUMO+1	-5.17	21	74 (N=N, 33)	05
LUMO	-5.57	13	81 (N=N, 46)	06
SOMO	-7.16	08	15	77
HOMO-1	-8.22	29	05	66
HOMO-2	-8.82	37	44	19
HOMO-3	-8.93	43	33	24
HOMO-4	-9.04	47	16	37
HOMO-5	-9.30	07	17	76
HOMO-6	-9.43	02	38	60
HOMO-7	-9.46	05	65	30
HOMO-8	-9.48	13	74	13
HOMO-9	-9.55	02	95	03
HOMO-10	-9.71	01	89	10
β -spin				
LUMO+5	-2.70	13	54	33
LUMO+4	-3.64	04	95	01
LUMO+3	-3.72	04	96	0
LUMO+2	-5.00	17	50 (N=N, 23)	33
LUMO+1	-5.28	16	51 (N=N, 24)	33
LUMO	-5.69	03	70 (N=N, 38)	27
HOMO	-7.99	21	03	76
HOMO-1	-8.77	39	43	18
HOMO-2	-8.80	49	27	24
HOMO-3	-8.98	51	17	32
HOMO-4	-9.22	05	20	75
HOMO-5	-9.40	02	45	53
HOMO-6	-9.43	04	53	43
HOMO-7	-9.47	12	77	11
HOMO-8	-9.54	02	96	02
HOMO-9	-9.71	01	90	09
HOMO-10	-10.05	10	25	65

Starting with the $[(\text{pap})_2\text{Ru}^{\text{II}}(\text{Q}^{\cdot-})]^+$ configuration at the native state in $1^+ - 4^+$ the one-electron oxidized EPR-silent $1^{2+} - 4^{2+}$ species could be defined either by the $[(\text{pap})_2\text{Ru}^{\text{III}}(\text{Q}^{\cdot-})]^{2+}$ formalism, where the unpaired spins on Ru^{III} and Q^{·-} are antiferromagnetically coupled, or by the individually spin-paired diamagnetic state of

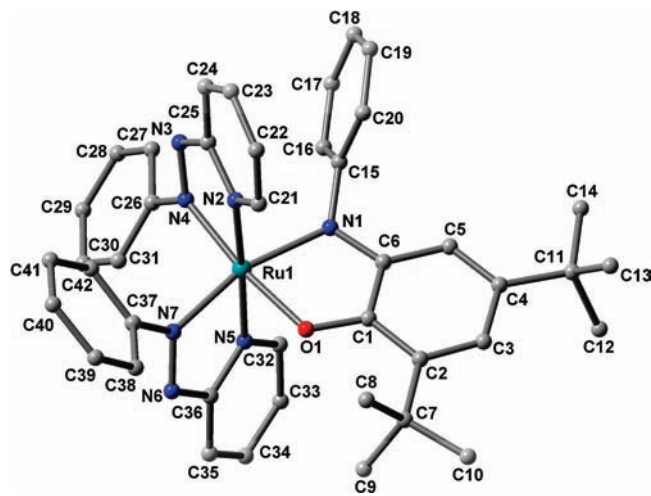
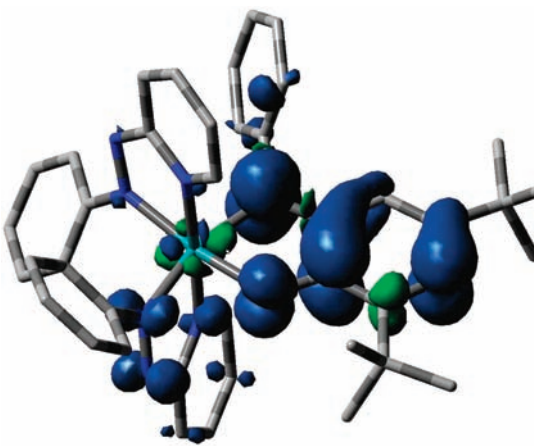
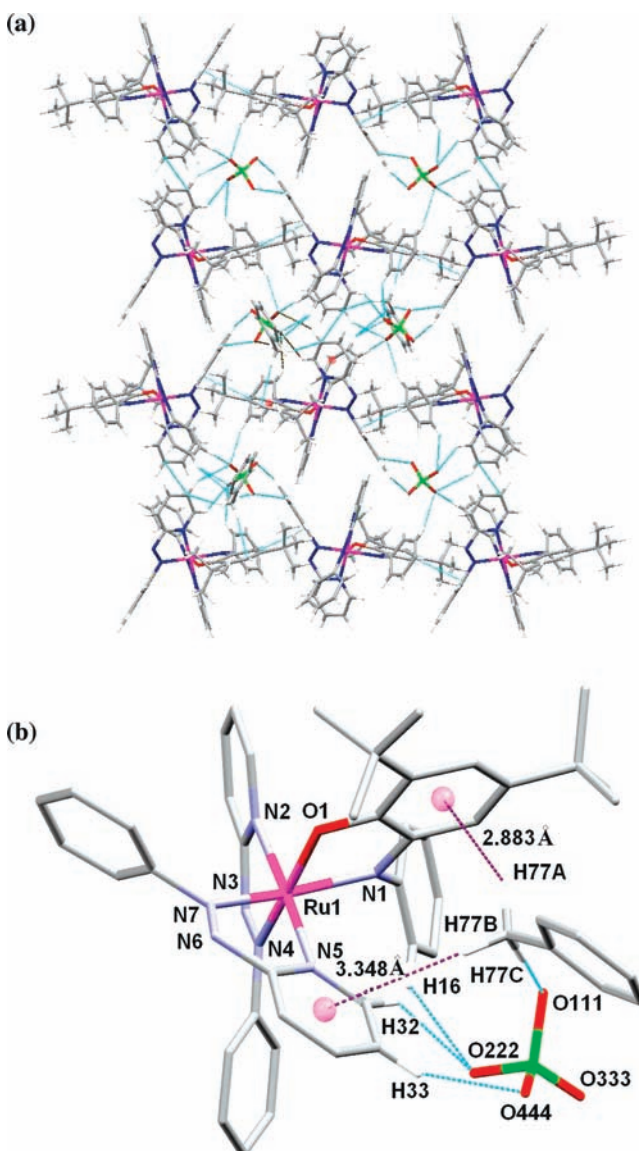
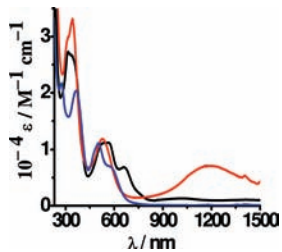
**Figure 2.** DFT-optimized structure of $[2]^+$.**Figure 3.** Spin density plot of $[2]^+$.**Figure 4.** (a) Packing diagram of $[2](\text{ClO}_4)\cdot\text{C}_7\text{H}_8$ along the a axis showing the hydrogen bonding and $\text{C}-\text{H}\cdots\pi$ networking. (b) A segment of the packing diagram highlighting hydrogen bondings and $\text{C}-\text{H}\cdots\pi$ interactions among $[2]^+$, ClO_4^- , and toluene.

Table 4. Hydrogen Bonding Parameters of $[2]\text{ClO}_4 \cdot \text{C}_7\text{H}_8$

D–H \cdots A ^a	d(D \cdots H) Å	d(H \cdots A) Å	d(D \cdots A) Å	\angle D–H \cdots A°
C(77)–H(77C) \cdots O(111)#1	0.98	2.570(5)	3.521(9)	163.65(5)
C(16)–H(16) \cdots O(222)#1	0.95	2.502(4)	3.303(6)	142.07(3)
C(32)–H(32) \cdots O(222)#1	0.95	2.481(4)	3.267(6)	140.1(3)
C(33)–H(33) \cdots O(444)#1	0.95	2.489(4)	3.324(6)	146.8(3)

^a#1: x, y, z.**Figure 5.** UV–vis–NIR spectral changes in CH_3CN for $[2]^n$ ($n = +2$ (blue), $+1$ (black), 0 (red)).

$[(\text{pap})_2\text{Ru}^{\text{II}}(\text{Q}^\circ)]^{2+}$. Though both of the formalisms are equally compatible as far as the EPR-silent state of the oxidized species is concerned,^{8a,b,23b,27} DFT calculations on the optimized $\mathbf{2}^+$ suggest that the SOMO is primarily dominated by the Q-based orbitals with 77% contribution along with minor participation from the Ru center, 8% (Table 3). Thus, under the present competitive scenario, the Q-based orbitals are preferentially involved in the oxidation process instead of a metal-based electron-transfer process leading to the $[(\text{pap})_2\text{Ru}^{\text{II}}(\text{Q}^\circ)]^{2+}$ configuration in $\mathbf{1}^{2+}\text{--}\mathbf{4}^{2+}$ along with the minor contribution from the alternate formulation of $[(\text{pap})_2\text{Ru}^{\text{III}}(\text{Q}^\bullet)]^{2+}$. Consequently, the low-energy band near 1000 nm due to interligand transition involving the SOMO of Q° and the LUMO+1 of pap in $[(\text{pap})_2\text{Ru}^{\text{II}}(\text{Q}^\bullet)]^+$ ($\mathbf{1}^+\text{--}\mathbf{4}^+$) disappears on preferential oxidation of Q^\bullet to the Q° state in $[(\text{pap})_2\text{Ru}^{\text{II}}(\text{Q}^\circ)]^{2+}$ ($\mathbf{1}^{2+}\text{--}\mathbf{4}^{2+}$). The $\{\text{Ru}^{\text{II}}\text{--}\text{Q}^\circ\}$ valence configuration of the oxidized species has also been revealed by the decrease in calculated C1–O1 and C6–N1 bond distances of Q to 1.264 and 1.317 Å, respectively,²⁰ in the optimized $\mathbf{2}^{2+}$ (Table 2). Moreover, the relatively weak interaction between the oxidized quinone state, Q° , and Ru(II) increases the Ru1–O1 and Ru1–N1 bond distances to 2.080 and 2.088 Å, respectively (Table 2), as evidenced previously in ruthenium–iminoquinone^{23b,27} and copper–quinone complexes.²⁸

The electrochemically generated $\mathbf{1}^{2+}\text{--}\mathbf{4}^{2+}$ exhibit two moderately intense visible energy bands near 600 and 500 nm, and the higher-energy visible band is associated with a shoulder near 470 nm (Figure 5, Table 5). The transitions can be assigned on the basis of TDDFT calculations on optimized $\mathbf{2}^{2+}$, λ/nm ($\epsilon/\text{M}^{-1}\text{cm}^{-1}$), 586.3 (1582), 517.6 (19913), and 475.7 (11987) (Table 6) [experimental: 588 (6640), 503 (11000), 476 (9500) (Table 5)], corresponding to HOMO/HOMO–1 \rightarrow LUMO+1, Ru(d π)/Q(π) \rightarrow pap(π^*); HOMO–1 \rightarrow LUMO+2, Ru(d π)/pap(π) \rightarrow pap(π^*) and HOMO–9 \rightarrow LUMO, Ru(d π)/Q(π) \rightarrow Q(π^*), respectively

(27) Masui, H.; Freda, A. L.; Zerner, M. C.; Lever, A. B. P. *Inorg. Chem.* **2000**, *39*, 141.(28) (a) Roy, S.; Sarkar, B.; Bubrin, D.; Niemeyer, M.; Zalis, S.; Lahiri, G. K.; Kaim, W. *J. Am. Chem. Soc.* **2008**, *130*, 15230. (b) Mukherjee, C.; Weyhermüller, T.; Bothe, E.; Chaudhuri, P. *Inorg. Chem.* **2008**, *47*, 2740.**Table 5.** Electronic Spectral Data of $[1]^n\text{--}[4]^n$ in CH_3CN

compound	$\lambda[\text{nm}] (\epsilon [\text{M}^{-1}\text{cm}^{-1}])$
$\mathbf{1}^{2+}$	601(10660), 496(8250), 456(6950), 366(16640), 268(17980)
$\mathbf{1}^+$	1016(1100), 665(5440), 564(8820), 533(8820), 342(20240), 318(20500)
1	1109(4940, 4050 cm^{-1} ^a), 570(6640), 533(8420), 334(26100), 307(23720)
$\mathbf{2}^{2+}$	588(6640), 503(11000), 476(9500), 366(20300), 273(21640)
$\mathbf{2}^+$	1003(1290), 665(6820), 565(11100), 528(11100), 339(26810), 316(27260)
2	1191(7180, 3890 cm^{-1} ^a), 560(9620), 527(11990), 342(33150), 308(29590)
$\mathbf{3}^{2+}$	602(8970), 510(11910), 476(9940), 360(21470), 281(25270)
$\mathbf{3}^+$	1018(1110), 668(5840), 572(9490), 533(9490), 341(21640), 312(22540)
3	1218(6370, 3810 cm^{-1} ^a), 565(7870), 525(9770), 344(26550), 309(24050)
$\mathbf{4}^{2+}$	581(9950), 507(8970), 472(7280), 367(14950), 275(16100)
$\mathbf{4}^+$	1002(1020), 668(4410), 563(8310), 537(8310), 346(18520), 312(20040)
4	1221(5220, 3650 cm^{-1} ^a), 561(7040), 523(8520), 339(22890), 309(21280)

^a Bandwidth at half height.

(Tables 6 and 8 and Figure 8). Though one moderately strong transition at 643.8(6698) has been predicted by TDDFT corresponding to HOMO–6 \rightarrow LUMO and Ru(d π)/Q(π) \rightarrow Q(π^*) (Table 6), it has not been resolved experimentally (Figure 5, Table 5)

Interestingly, the visible-region transitions originate from the filled mixed metal(Ru)/ligand(Q or pap)-based orbitals to the empty pap- or Q-based orbitals as MLLCT (metal/ligand-to-ligand charge transfer) bands. This is due to the fact that the filled MOs in the oxidized state of $\mathbf{2}^{2+}$ are primarily dominated by the Q- or pap-based orbitals with partial mixing of Ru orbitals (HOMO–HOMO–5), and the LUMOs (LUMO–LUMO+4) are centered around Q and pap with a slight percentage of Ru. In the oxidized $[(\text{pap})_2\text{Ru}^{\text{II}}(\text{Q}^\circ)]^{2+}$ ($\mathbf{1}^{2+}\text{--}\mathbf{4}^{2+}$), the LUMO is dominated by the Q $^\circ$ -based orbitals (81%; Table 8), implying stronger π -acceptor character of Q° relative to pap, which in turn results in a lowest-energy MLLCT transition, Ru(d π)/Q(π) \rightarrow Q(π^*) at 643.8 nm. However, the higher-energy LUMOs (LUMO+1 to LUMO+4) are composed of pap-based orbitals (Table 8).

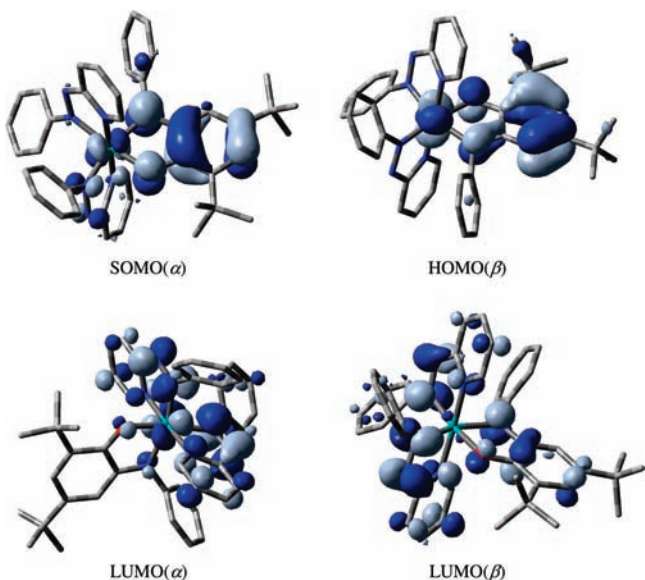
The presence of two sets of strongly π -acceptor ligands (Q $^\circ$ and pap) in $[(\text{pap})_2\text{Ru}^{\text{II}}(\text{Q}^\circ)]^{2+}$ ($\mathbf{1}^{2+}\text{--}\mathbf{4}^{2+}$) stabilizes the Ru(II) state to a large extent such that appreciable Ru contribution (44%) has been calculated along with the pap and Q contributions of 16% and 40%, respectively, only in the deep down HOMO–6 state (Table 8). The immediate consequence of this effect is that no further oxidation of Ru(II)–Q $^\circ$ to Ru(III)–Q $^\circ$ has been detected by cyclic voltammetry within +2.0 V versus SCE (Figure 7, Table 7) as otherwise anticipated. It may be noted that the Ru(II)/(III) couple in $[\text{Ru}(\text{pap})_3]^{2+}$ with three strongly π -accepting

Table 6. Selected Visible Energy Transitions at the TD-DFT/B3LYP/6-31G(d) Level for $\mathbf{2}^+$, $\mathbf{2}^{2+}$, and $\mathbf{2}$

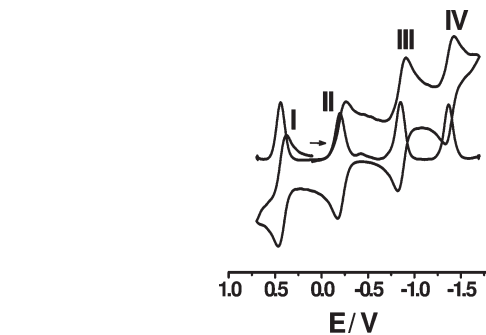
For $\mathbf{2}^{2+}$					
excited state	λ/nm	oscillator strength	$\varepsilon/\text{M}^{-1}\text{cm}^{-1}$	key transitions	character
1	1328.8	0.0131	2921	(96%) SOMO(α) \rightarrow LUMO(α)	$Q(\pi) \rightarrow \text{pap}(\pi^*)$
2	998.4	0.0120	2676	(94%) SOMO(α) \rightarrow LUMO+1(α)	$Q(\pi) \rightarrow \text{pap}(\pi^*)$
7	652.5	0.0045	1003	(21%) HOMO-1(α) \rightarrow LUMO+1(α) (20%) HOMO-2(α) \rightarrow LUMO(α) (17%) HOMO-1(α) \rightarrow LUMO(α)	$\text{Ru}(d\pi)/Q(\pi) \rightarrow \text{pap}(\pi^*)$ $\text{Ru}(d\pi)/\text{pap}(\pi) \rightarrow \text{pap}(\pi^*)$ $\text{Ru}(d\pi)/Q(\pi) \rightarrow \text{pap}(\pi^*)$
11	549.3	0.0391	8718	(22%) HOMO-2(β) \rightarrow LUMO(β) (20%) HOMO-3(β) \rightarrow LUMO+1(β) (17%) HOMO-1(β) \rightarrow LUMO(β)	$\text{Ru}(d\pi) \rightarrow \text{pap}(\pi^*)$ $\text{Ru}(d\pi) \rightarrow \text{pap}(\pi^*)$ $\text{Ru}(d\pi)/\text{pap}(\pi) \rightarrow \text{pap}(\pi^*)$
12	541.0	0.0403	8986	(25%) HOMO-2(β) \rightarrow LUMO(β) (17%) HOMO-2(β) \rightarrow LUMO+2(β)	$\text{Ru}(d\pi) \rightarrow \text{pap}(\pi^*)$ $\text{Ru}(d\pi) \rightarrow \text{pap}(\pi^*)$

For $\mathbf{2}^{2+}$					
excited state	λ/nm	oscillator strength	$\varepsilon/\text{M}^{-1}\text{cm}^{-1}$	key transitions	character
7	643.8	0.0470	6698	(62%) HOMO-6 \rightarrow LUMO	$\text{Ru}(d\pi)/Q(\pi) \rightarrow Q(\pi^*)$
10	586.3	0.0111	1582	(45%) HOMO \rightarrow LUMO+1	$\text{Ru}(d\pi)/Q(\pi) \rightarrow \text{pap}(\pi^*)$
11	517.6	0.1355	19913	(22%) HOMO-1 \rightarrow LUMO+1 (53%) HOMO-1 \rightarrow LUMO+2	$\text{Ru}(d\pi)/\text{pap}(\pi) \rightarrow \text{pap}(\pi^*)$ $\text{Ru}(d\pi)/\text{pap}(\pi) \rightarrow \text{pap}(\pi^*)$
12	475.7	0.0841	11987	(51%) HOMO-9 \rightarrow LUMO	$\text{Ru}(d\pi)/Q(\pi) \rightarrow Q(\pi^*)$

For $\mathbf{2}$					
excited state	λ/nm	oscillator strength	$\varepsilon/\text{M}^{-1}\text{cm}^{-1}$	key transitions	character
1	1301.5	0.0249	1597	(53%) HOMO \rightarrow LUMO	$\text{pap}(\pi)/Q(\pi) \rightarrow \text{pap}(\pi^*)$
2	1040.9	0.0881	5651	(56%) HOMO \rightarrow LUMO+1	$\text{pap}(\pi)/Q(\pi) \rightarrow \text{pap}(\pi^*)$
6	561.7	0.0410	2630	(95%) HOMO \rightarrow LUMO+3	$\text{pap}(\pi)/Q(\pi) \rightarrow \text{pap}(\pi^*)$
7	519.5	0.0335	2149	(47%) HOMO-2 \rightarrow LUMO (26%) HOMO-3 \rightarrow LUMO	$\text{Ru}(d\pi)/\text{pap}(\pi)/Q(\pi) \rightarrow \text{pap}(\pi^*)$ $\text{Ru}(d\pi)/\text{pap}(\pi)/Q(\pi) \rightarrow \text{pap}(\pi^*)$

**Figure 6.** Contour plots of the selective frontier molecular orbitals for $\mathbf{2}^+$.

ligands has been reported to take place at +2.22 V versus SCE in CH_3CN .²⁹ The presence of 10–15% Ru contribution in the LUMOs (up to LUMO+4; Table 8) suggests reasonable mixing of metal–ligand ($\text{Q}^\circ/\text{pap}$) frontier orbitals in $\mathbf{1}^{2+}-\mathbf{4}^{2+}$ as in the native states of $\mathbf{1}^+-\mathbf{4}^+$.

**Figure 7.** Cyclic and differential pulse voltammograms of $[\mathbf{2}]^+$ in CH_3CN . The potentials are represented against SCE as a reference.

The one-electron reduction of the native $[(\text{pap})_2\text{Ru}^{\text{II}}(\text{Q}^\bullet^-)]^+$ ($\mathbf{1}^+-\mathbf{4}^+$) also yields an EPR-silent state, which is equally compatible with the two possible formalisms of either the doubly reduced spin-paired catecholato form in $[(\text{pap})_2\text{Ru}^{\text{II}}(\text{Q}^2^-)]$ ($\mathbf{1}-\mathbf{4}$) or selective reduction of the azo ($\text{N}=\text{N}$) function of one of the pap ligands, resulting in $[(\text{pap})(\text{pap}^\bullet^-)\text{Ru}^{\text{II}}(\text{Q}^\bullet^-)]$ ($\mathbf{1}-\mathbf{4}$), where the unpaired spins on the radical state of pap^\bullet^- and Q^\bullet^- are antiferromagnetically coupled. The reduction of the azo function of pap is equally feasible, as with the redox noninnocent quinone (Q^\bullet^-) center in $[(\text{pap})_2\text{Ru}^{\text{II}}(\text{Q}^\bullet^-)]^+$ ($\mathbf{1}^+-\mathbf{4}^+$), due to its ability to accept a maximum of two electrons in the low-lying vacant π^* orbitals.¹⁴ However, DFT results on $\mathbf{2}^+$ predict that the LUMO(β) is composed of 27% Q and a total 38% reducible azo($\text{N}=\text{N}$) function of two pap ligands, that is, 19% azo contribution from each of the pap ligands (Table 3, Figure 6).

Table 7. Redox Potentials^a and Comproportionation Constant Values of $[1]^{+}$ – $[4]^{+}$

compound	$E^{\circ}_{298}[\text{V}] (\Delta E_p [\text{mV}])$							
	couple I	couple II	couple III	couple IV	K_{c1}^b	K_{c2}^b	K_{c3}^b	
$[1]^{+}$	0.50(60)	-0.11(70)	-0.78(70)	-1.26(130)	$10^{10.3}$	$10^{11.4}$	$10^{8.1}$	
$[2]^{+}$	0.46(80)	-0.17(80)	-0.82(70)	-1.34(80)	$10^{10.7}$	$10^{11.0}$	$10^{8.8}$	
$[3]^{+}$	0.43(60)	-0.20(80)	-0.85(80)	-1.38(110)	$10^{10.7}$	$10^{11.0}$	$10^{8.9}$	
$[4]^{+}$	0.39(80)	-0.23(80)	-0.90(80)	-1.44(90)	$10^{10.5}$	$10^{11.5}$	$10^{9.1}$	

^a Potentials E°_{298} [V] (ΔE_p [mV]) versus SCE; in $\text{CH}_3\text{CN}/0.1 \text{ M}$ Et_4NClO_4 ; scan rate, 100 mV s⁻¹. ^b $RT \ln K_c = nF(\Delta E)$. K_{c1} , K_{c2} , and K_{c3} correspond to successive first oxidation and first reduction processes, the first and second reduction processes, and the second and third reduction processes, respectively.

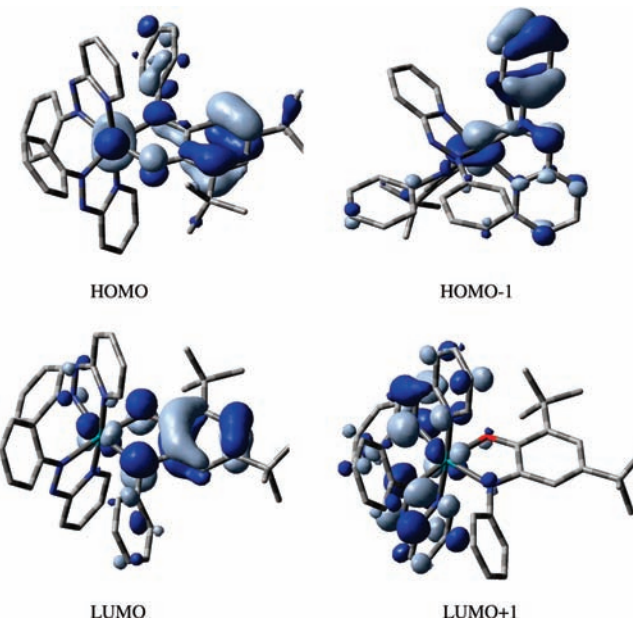
Table 8. Selected Molecular Orbitals Along with Their Energies and Compositions for $[2]^{2+}$

MO	energy, eV	composition		
		Ru	Pap	Q
LUMO+5	-6.14	47	19	34
LUMO+4	-6.49	03	96	01
LUMO+3	-6.57	04	96	0
LUMO+2	-8.21	14	84 (N=N, 39)	02
LUMO+1	-8.43	07	89 (N=N, 47)	04
LUMO	-9.12	09	10	81
HOMO	-11.32	27	04	69
HOMO-1	-11.60	20	70	10
HOMO-2	-11.70	14	81	05
HOMO-3	-11.80	04	93	03
HOMO-4	-11.92	15	67	18
HOMO-5	-11.94	21	68	11
HOMO-6	-11.99	44	16	40
HOMO-7	-12.02	46	38	16
HOMO-8	-12.17	05	18	77
HOMO-9	-12.30	21	09	70
HOMO-10	-13.03	03	28	69

Therefore, the first reduced state (**1–4**) is likely to hold the valence structure of $[(\text{pap})_2\text{Ru}^{\text{II}}(\text{Q}^{2-})]$ instead of the alternate form of $[(\text{pap})(\text{pap}^{\bullet-})\text{Ru}^{\text{II}}(\text{Q}^{\bullet-})]$. This finds further justification as the HOMO of the optimized reduced **2** is indeed dominated by the Q-based orbitals with 64% contribution (Table 9, Figure 9). In accordance with this, the calculated bond distances of coordinated Q in the optimized structure of **2**, C1–O1 = 1.337, C6–N1 = 1.390, C1–C2 = 1.407, C2–C3 = 1.394, C3–C4 = 1.408, C4–C5 = 1.393, C5–C6 = 1.415, and C6–C1 = 1.432 Å (Table 2), are comparable with the doubly reduced Q^{2-} state,^{8d,20} whereas the calculated N3–N4 (1.299) and N6–N7 (1.306 Å) (Table 2) distances of the pap ligands in **2** remain close to the neutral N=N form as in the native (**2**⁺) and first oxidized (**2**²⁺) states.

The gradual slight increase of the calculated N=N distances of pap ligands, 1.274/1.269 Å in **2**²⁺ to 1.297/1.289 Å in **2**⁺ to 1.299/1.306 Å in **2** (Table 2), reveals that the extent of transfer of charge from the (d π)Ru(II) to the $\pi^*(\text{N}=\text{N})$ of pap increases with the increase in electron density on Q, $\text{Q}^{\bullet}\rightarrow\text{Q}^{\bullet}\rightarrow\text{Q}^{2-}$.

The reduced $[(\text{pap})_2\text{Ru}^{\text{II}}(\text{Q}^{2-})]$, **1–4**, display one moderately intense broad near-IR band in the range of 1100–1200 nm with a bandwidth at half height, $\Delta\nu_{1/2}$, of $\sim 4000 \text{ cm}^{-1}$ (Table 5, Figure 5). The peak position of this broad band is sensitive to the electronic nature of the R group in the framework of Q, and its energy (ν/cm^{-1}) decreases systematically with the increasing

**Figure 8.** Contour plots of the selective frontier molecular orbitals for **2**²⁺.**Table 9.** Selected Molecular Orbitals Along with Their Energies and Compositions for **2**

MO	energy, eV	composition		
		Ru	Pap	Q
LUMO+5	-0.13	21	56	23
LUMO+4	-0.25	08	79	13
LUMO+3	-0.74	04	96	0
LUMO+2	-0.97	04	96	0
LUMO+1	-2.47	18	70 (N=N, 31)	12
LUMO	-2.73	17	68 (N=N, 34)	15
HOMO	-3.79	03	33	64
HOMO-1	-4.91	17	02	81
HOMO-2	-5.71	44	40	16
HOMO-3	-5.84	55	24	21
HOMO-4	-5.94	59	14	27
HOMO-5	-6.18	05	11	84
HOMO-6	-6.43	07	88	05
HOMO-7	-6.53	01	04	95
HOMO-8	-6.63	04	88	08
HOMO-9	-6.80	01	98	01
HOMO-10	-6.97	03	88	09

electron-donating nature of R. It follows the order **1**⁺ > **2**²⁺ > **3**⁺ > **4**⁺. The TDDFT calculations on the optimized reduced **2** predict two low-energy interligand transitions, λ/nm ($\epsilon/\text{M}^{-1}\text{cm}^{-1}$), at 1301.5(1597) and 1040.9(5651) (Tables 6 and 9) corresponding to HOMO \rightarrow LUMO and pap(π)/Q(π) \rightarrow pap(π^*) and to HOMO \rightarrow LUMO+1 and pap(π)/Q(π) \rightarrow pap(π^*), respectively, (Table 6); however, only one broad near-IR transition centered at 1191 (7180) has been resolved (Table 5, Figure 5). The reduced complexes (**1–4**) also exhibit one intense transition in the visible region between 520 and 530 nm associated with a shoulder at the lower-energy part near 560 nm (Table 5, Figure 5). The TDDFT calculations on **2** predict two transitions, λ/nm ($\epsilon/\text{M}^{-1}\text{cm}^{-1}$), at 561.7 (2630) and 519.5 (2149) (experimental: 560 (9620) and 527 (11990)) corresponding to HOMO \rightarrow LUMO+3 and pap(π)/Q(π) \rightarrow pap(π^*) and to HOMO-2/HOMO-3 \rightarrow LUMO and Ru(d π)/pap(π)/Q(π) \rightarrow pap(π^*) (Tables 6 and 9). The 17–18% Ru contribution in the lower-energy LUMOs (LUMO and LUMO+1, Table 9)

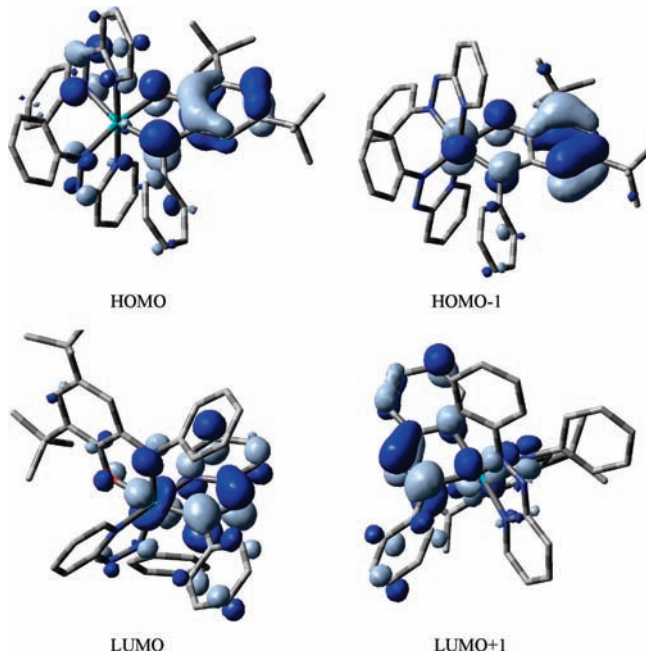


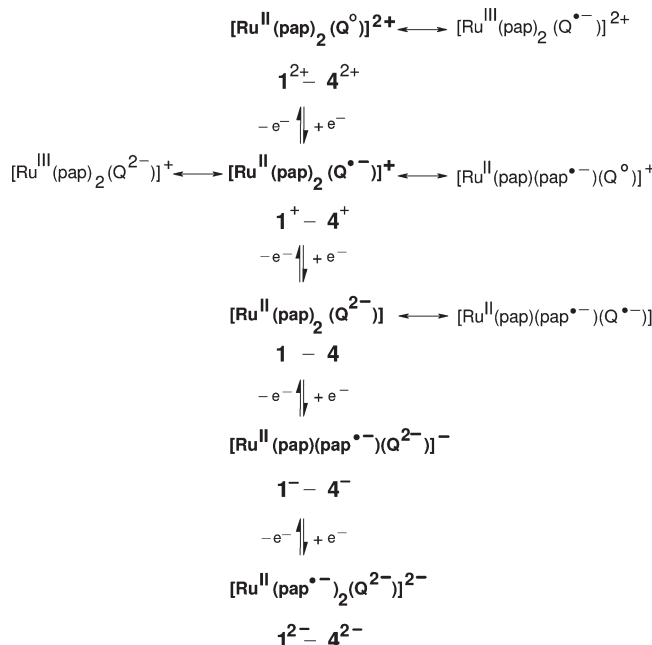
Figure 9. Contour plots of the selective frontier molecular orbitals for **2**.

justifies partial metal–ligand mixing as calculated in the native **1⁺–4⁺** (Table 3) and oxidized **1²⁺–4²⁺** (Table 8) states.

Though the further two successive reductions, couple III, **1⁻–4⁻**, and couple IV, **1²⁻–4²⁻**, are quasi-reversible on the cyclic voltammetric time scale (Figure 7), the electrochemically generated second and third reduced states are unstable on the coulometric time scale at 298 K, which has precluded to follow the spectral changes on second and third reductions. In **2**, Q exists in fully reduced Q^{2-} state, and Ru^{II} is most unlikely to get reduced further to Ru(I) . The azo functions of pap ligands are therefore the obvious subsequent reduction sites. The DFT calculations on the optimized native **2⁺** and first reduced **2** (Tables 3 and 9) accordingly suggest the pap-dominated higher-energy LUMOs (LUMO+1 onward).

In conclusion, the presence of two sets of noninnocent ligands, Q and pap, along with the redox-active Ru ion in the complexes **[1]ⁿ–[4]ⁿ** introduces multiple resonating valence structure alternatives of the complexes in the native as well as oxidized and reduced states, as shown in Scheme 3. The experimental and DFT calculations convincingly establish the following: (i) A preferential stabilization of the paramagnetic $\{\text{(pap)}_2\text{-Ru}^{\text{II}}-\text{Q}^{\bullet-}\}$ configuration in the native state, **[1]⁺–[4]⁺**, which in effect exhibits low-energy near-IR interligand transitions involving singly occupied $\pi(\text{Q})$ and empty $\pi^*(\text{pap})$ orbitals. (ii) Selective oxidation of the semi-quinone moiety ($\text{Q}^{\bullet-}$) leads to the diamagnetic $\{\text{(pap)}_2\text{-Ru}^{\text{II}}-\text{Q}^{\circ}\}$ formalism in **[1]²⁺–[4]²⁺**, and the influence of two sets of strong π -acceptor ligands, pap and Q[°], stabilizes the Ru(II) state in **[1]²⁺–[4]²⁺** to a great extent, such that the expected $\text{Ru(II)} \rightarrow \text{Ru(III)}$ oxidation does not take place within +2.0 V versus SCE. (iii) The preferential first reduction of $\text{Q}^{\bullet-}$ to Q^{2-} results in the diamagnetic $\{\text{(pap)}_2\text{-Ru}^{\text{II}}-\text{Q}^{2-}\}$ state in **1–4**, which in turn displays one broad interligand transition at the near-IR region corresponding to $\text{pap}(\pi)/\text{Q}(\pi) \rightarrow \text{pap}(\pi^*)$. (iv) The subsequent second and third reductions expectedly take place at the pap sites. (v) In the present $\{\text{(pap)}_2\text{-Ru-Q}\}$ setup, the Q- or pap-based orbitals essentially participate in the electron-transfer

Scheme 3. Preferred Valence Combination Is Shown in Boldface



processes, leaving the +2 formal charge of ruthenium unaltered (Scheme 3). The present work therefore once again demonstrates the built-in sensitivities of the valence structures of the ruthenium–quinonoid complexes, which emphasizes the need for further scrutiny with the newer challenging molecular frameworks.

Experimental Section

The precursor complex *cis,trans,cis*-Ru(pap)₂(Cl)₂³⁰ and the substituted 2-anilino-4,6-di-tert-butylphenol(H₂Q) were prepared according to the reported procedures.^{13b,31} Other chemicals and solvents were of reagent grade and used as received. For spectroscopic and electrochemical studies, HPLC-grade solvents were used.

UV-vis–NIR spectra in CH₃CN/0.1 M Et₄NClO₄ at 298 K were recorded on a Perkin-Elmer 950 lambda spectrophotometer. FT-IR spectra were taken on a Nicolet spectrophotometer with samples prepared as KBr pellets. Solution electrical conductivity was checked using a Systronic 304 conductivity bridge. The EPR measurements were made with a Varian model 109C E-line X-band spectrometer fitted with a quartz dewar at 77 K. Cyclic voltammetric, differential pulse voltammetric, and coulometric measurements were carried out using a PAR model 273A electrochemistry system. Platinum wire working and auxiliary electrodes and an aqueous SCE were used in a three-electrode configuration. The supporting electrolyte was 0.1 M [NEt₄]ClO₄, and the solute concentration was $\sim 10^{-3}$ M. The half-wave potential E°_{298} was set equal to 0.5 ($E_{\text{pa}} + E_{\text{pc}}$), where E_{pa} and E_{pc} are the anodic and cathodic cyclic voltammetric peak potentials, respectively. A platinum wire-gauze working electrode was used in the coulometric experiments. The elemental analyses were carried out with a Perkin-Elmer 240C elemental analyzer. Electrospray mass spectra were recorded on a Micromass Q-ToF mass spectrometer.

Caution! Perchlorate salts of metal complexes with organic ligands are potentially explosive. Heating of dried samples must

(30) Goswami, S.; Chakravarty, A. R.; Chakravorty, A. *Inorg. Chem.* **1981**, *20*, 2246.

(31) Mukherjee, S.; Weyhermüller, T.; Bothe, E.; Wieghardt, K.; Chaudhuri, P. *Dalton Trans.* **2004**, 3842.

be avoided; handling of small amounts has to proceed with great caution using protection.

Preparation of Complexes [1]ClO₄–[4]ClO₄. The complexes [1]ClO₄–[4]ClO₄ were prepared by following a general procedure. The details are given for one representative complex, [2]ClO₄.

[Ru(pap)₂(Q²)]ClO₄, [2]ClO₄. The starting complex *cis,trans*, *cis*-Ru(pap)₂(Cl)₂ (100 mg, 0.186 mmol) and excess AgClO₄ (154 mg, 0.74 mmol) were heated to reflux in 10 mL of ethanol for 2 h under a dinitrogen atmosphere. The precipitated AgCl was filtered off, which resulted in a red–violet solution of [Ru(pap)₂(EtOH)₂]²⁺. To this were added ligand 2-anilino-4,6-ditert-butylphenol(H₂Q²) (83 mg, 0.279 mmol) and a few drops of NEt₃, and the mixture was refluxed for 12 h under a dinitrogen atmosphere. The purple solution was evaporated to dryness under reduced pressure, and the solid mass was purified by column chromatography using a silica gel column (60–120 mesh). The desired violet band was eluted by CH₂Cl₂–CH₃CN (5:1). On removal of the solvent under reduced pressure, the pure complex [2]ClO₄ was obtained as a dark-colored solid, which was further dried under a vacuum.

[1]ClO₄. Yield: 130 mg (75%). C₄₂H₄₁N₇O₅Cl₃Ru Anal. Calcd (Found): C, 54.19 (54.23); H, 4.44 (4.12); N, 10.54 (10.63). ESI MS (in CH₃CN) *m/z* Calcd (Found) for [1]⁺: 831.18 (831.67). Molar conductivity [Λ_M/Ω^{-1} cm² M⁻¹] in acetonitrile: 110.

[2]ClO₄. Yield: 117 mg (73%). C₄₂H₄₃N₇O₅ClRu Anal. Calcd (Found): C, 58.45 (58.20); H, 5.03 (5.17); N, 11.37 (11.11). ESI MS (in CH₃CN) *m/z* Calcd (Found) for [2]⁺: 763.26 (763.39). Molar conductivity [Λ_M/Ω^{-1} cm² M⁻¹] in acetonitrile: 132.

[3]ClO₄. Yield: 127 mg (74%). C₄₄H₄₇N₇O₇ClRu Anal. Calcd (Found): C, 57.25 (57.33); H, 5.14 (5.19); N, 10.63 (10.82). ESI MS (in CH₃CN) *m/z* Calcd (Found) for [3]⁺: 823.28 (823.07). Molar conductivity [Λ_M/Ω^{-1} cm² M⁻¹] in acetonitrile: 120.

(32) Sheldrick, G. M. *SHELX-97*; Program for Crystal Structure Solution and Refinement, University of Göttingen: Göttingen, Germany, 1997.

(33) Lee, C.; Yang, W.; Parr, R. G. *Phys. Rev. B* **1988**, *37*, 785.

(34) (a) Andrae, D.; Haeussermann, U.; Dolg, M.; Stoll, H.; Preuss, H. *Theor. Chim. Acta* **1990**, *77*, 123. (b) Fuentealba, P.; Preuss, H.; Stoll, H.; Szentpaly, L. V. *Chem. Phys. Lett.* **1989**, *89*, 418.

(35) Frisch, M. J.; Trucks, G. W.; Schlegel, H. B.; Scuseria, G. E.; Robb, M. A.; Cheeseman, J. R.; Montgomery, J. A.; Vreven, T. Jr.; Kudin, K. N.; Burant, J. C.; Millam, J. M.; Iyengar, S. S.; Tomasi, J.; Barone, V.; Mennucci, B.; Cossi, M.; Scalmani, G.; Rega, N.; Petersson, G. A.; Nakatsuji, H.; Hada, M.; Ehara, M.; Toyota, K.; Fukuda, R.; Hasegawa, J.; Ishida, M.; Nakajima, T.; Honda, Y.; Kitao, O.; Nakai, H.; Klene, M.; Li, X.; Knox, J. E.; Hratchian, H. P.; Cross, J. B.; Bakken, V.; Adamo, C.; Jaramillo, J.; Gomperts, R.; Stratmann, R. E.; Yazyev, O.; Austin, A. J.; Cammi, R.; Pomelli, C.; Ochterski, J. W.; Ayala, P. Y.; Morokuma, K.; Voth, G. A.; Salvador, P.; Dannenberg, J. J.; Zakrzewski, V. G.; Dapprich, S.; Daniels, A. D.; Strain, M. C.; Farkas, O.; Malick, D. K.; Rabuck, A. D.; Raghavachari, K.; Foresman, J. B.; Ortiz, J. V.; Cui, Q.; Baboul, A. G.; Clifford, S.; Cioslowski, J.; Stefanov, B. B.; Liu, G.; Liashenko, A.; Piskorz, P.; Komaromi, I.; Martin, R. L.; Fox, D. J.; Keith, T.; Al-Laham, M. A.; Peng, C. Y.; Nanayakkara, A.; Challacombe, M.; Gill, P. M. W.; Johnson, B.; Chen, W.; Wong, M. W.; Gonzalez, C.; Pople, J. A. *Gaussian 03*, Gaussian, Inc.: Wallingford, CT, 2004.

[4]ClO₄. Yield: 132 mg (72%). C₅₀H₅₉N₇O₅ClRu Anal. Calcd. (Found): C, 61.58 (61.32); H, 6.10 (6.02); N, 10.06 (9.99). ESI MS (in CH₃CN) *m/z* Calcd (Found) for [4]⁺: 875.38 (875.52). Molar conductivity [Λ_M/Ω^{-1} cm² M⁻¹] in acetonitrile: 130.

Crystal Structure Determination of [2]ClO₄·C₇H₈. Single crystals were grown by slow evaporation of a 1:1 acetonitrile–toluene mixture of [2]ClO₄. X-ray data for [2]ClO₄ were collected using an OXFORD XCALIBUR-S CCD single-crystal X-ray diffractometer. The structure was solved and refined using full-matrix least-squares techniques on *F*² using the SHELX-97 program.³² The absorption corrections were done using multi-scan (SHELXTL program package), and all of the data were corrected for Lorentz polarization effects. Hydrogen atoms were included in the refinement process as per the riding model. The X-ray structural analysis reveals the presence of one toluene molecule as the solvent of crystallization in the asymmetric unit.

Computational Details. Full geometry optimizations were carried out using the density functional theory method at the (U)B3LYP level for 2⁺ and the (R)B3LYP level for 2²⁺ and 2.³³ All elements except ruthenium were assigned the 6-31G(d) basis set. The SDD basis set with effective core potential was employed for the ruthenium atom.³⁴ The vibrational frequency calculations were performed to ensure that the optimized geometries represent the local minima, and there are only positive Eigen values. All calculations were performed with the Gaussian03 program package.³⁵ Vertical electronic excitations based on B3LYP-optimized geometries were computed for the TDDFT formalism³⁶ in acetonitrile using the conductor-like polarizable continuum model.³⁷ GaussSum³⁸ was used to calculate the fractional contributions of various groups to each molecular orbital.

Acknowledgment. Financial support received from the Department of Science and Technology and the University Grant Commission (India) is gratefully acknowledged. X-ray structural studies for [2]ClO₄ were carried out at the National Single Crystal Diffractometer Facility, Indian Institute of Technology, Bombay. Special acknowledgment is made to the Sophisticated Analytical Instrument Facility (SAIF), Indian Institute of Technology Bombay, for providing the EPR facility.

Supporting Information Available: X-ray crystallographic file in CIF format for [2]ClO₄·C₇H₈; EPR spectra in CH₃CN at 77 K and in the polycrystalline state at 298 and 77 K (Figure S1). This material is available free of charge via the Internet at <http://pubs.acs.org>.

(36) (a) Bauernschmitt, R.; Ahlrichs, R. *Chem. Phys. Lett.* **1996**, *256*, 454. (b) Stratmann, R. E.; Scuseria, G. E.; Frisch, M. J. *J. Chem. Phys.* **1998**, *109*, 8218. (c) Casida, M. E.; Jamorski, C.; Casida, K. C.; Salahub, D. R. *J. Chem. Phys.* **1998**, *108*, 4439.

(37) (a) Barone, V.; Cossi, M. *J. Phys. Chem. A* **1998**, *102*, 1995. (b) Cossi, M.; Barone, V. *J. Chem. Phys.* **2001**, *115*, 4708. (c) Cossi, M.; Rega, N.; Scalmani, G.; Barone, V. *J. Comput. Chem.* **2003**, *24*, 669.

(38) O'Boyle, N. M.; Tenderholt, A. L.; Langner, K. M. *J. Comput. Chem.* **2008**, *29*, 839.